

Article

Nitrogen and Sulfur Co-Doped Graphene Quantum Dots Anchored TiO₂ Nanocomposites for Enhanced Photocatalytic Activity

Jishu Rawal¹, Urooj Kamran^{1,2}, Mira Park^{3,4} , Bishweshwar Pant^{3,4,*}  and Soo-Jin Park^{1,*}

¹ Department of Chemistry, Inha University, 100 Inharo, Incheon 22212, Korea; rawaljishu26@gmail.com (J.R.); malikurooj9@gmail.com (U.K.)

² Department of Mechanical Engineering, College of Engineering, Kyung Hee University, Yongin 17104, Korea

³ Carbon Composite Energy Nanomaterials Research Center, Woosuk University, Wanju, Chonbuk 55338, Korea; wonderfulmira@woosuk.ac.kr

⁴ Woosuk Institute of Smart Convergence Life Care (WSCLC), Woosuk University, Wanju, Chonbuk 55338, Korea

* Correspondence: bisup@woosuk.ac.kr (B.P.); sjpark@inha.ac.kr (S.-J.P.)

Abstract: Herein, nitrogen (N) and sulfur (S) co-doped graphene quantum dots (GQDs) using different one-dimensional (1-D) carbon nanomaterials as precursors were synthesized, followed by heterojunction formation with TiO₂. GQDs exhibit unlike physiochemical properties due to the disproportionate ratio of N and S heteroatoms and dissimilar reaction parameters. Tailored type-II band gap (E_g) alignment was formed with narrowed E_g value that improves photogenerated electron transfer due to π -conjugation. GQDs-TiO₂ nanocomposites exhibit remarkably high methylene blue (MB) degradation up to 99.78% with 2.3–3 times elevated rate constants as compared with TiO₂. CNF-GQDs-TiO₂ demonstrates the fastest MB degradation (60 min) due to the synergistic effect of nitrogen and sulfur doping, and is considered the most stable photocatalyst among prepared nanocomposites as tested up to three cyclic runs. Whereas, C–O–Ti bonds were not only responsible for nanocomposites strengthening but also provide a charge transfer pathway. Moreover, charge transport behavior, generation of active species, and reaction mechanism were scrutinized via free-radical scavenger analysis.

Keywords: photocatalytic degradation; graphene quantum dots; nanocomposites; free radical generation



Citation: Rawal, J.; Kamran, U.; Park, M.; Pant, B.; Park, S.-J. Nitrogen and Sulfur Co-Doped Graphene Quantum Dots Anchored TiO₂ Nanocomposites for Enhanced Photocatalytic Activity. *Catalysts* **2022**, *12*, 548. <https://doi.org/10.3390/catal12050548>

Academic Editor: John Vakros

Received: 10 April 2022

Accepted: 11 May 2022

Published: 17 May 2022

Publisher's Note: MDPI stays neutral with regard to jurisdictional claims in published maps and institutional affiliations.



Copyright: © 2022 by the authors. Licensee MDPI, Basel, Switzerland. This article is an open access article distributed under the terms and conditions of the Creative Commons Attribution (CC BY) license (<https://creativecommons.org/licenses/by/4.0/>).

1. Introduction

Environmental catastrophes and energy crises have become the main challenges in recent decades because of their severe social and economic impact on humankind [1,2]. Heterogeneous photocatalysis has recently attracted enormous attention because of its green attributes and efficient applicability. Due to their favorable properties such as suitable bandgaps, good chemical stability, and strong oxidizing ability, semiconductor photocatalysts [3–5] (e.g., ZnO, WO₃, CdS, CdSe, PbS, TiO₂, and SnO₂) and some biocomposites [6,7] have been extensively used to decompose organic pollutants [8]. Among the semiconductor photocatalysts, titanium dioxide (TiO₂) appears to be a highly efficient, stable, nontoxic, and inexpensive photocatalyst [9,10]. TiO₂ containing 80% anatase and 20% rutile, named Degussa P25 TiO₂, is widely known to exhibit high performance because the mixed-phase material exhibits a slower recombination rate, higher photo efficiency, and lower light activation energy as compared with pure-phase anatase or rutile [11,12]. Despite its wide range of applications, good performance, and high stability, the use of TiO₂ is restricted by its narrow ultraviolet light range response resulting from the intrinsic wide energy bandgap of the anatase phase [13] and its low quantum efficiency due to the high recombination rate of photogenerated charge carriers in the rutile phase [14].

Various methods have been used to further expand the optical UV-vis absorption region of TiO₂ and to enhance the efficient light-induced charge separation. Numerous approaches to modifying TiO₂ via doping [15,16], semiconductor coupling [17], composite formation with carbon nanomaterials [18–21], and chemical treatment [22] have been explored to overcome the aforementioned shortcomings [23]. The best option reported thus far for spanning the UV-vis spectrum is combining TiO₂ with typical narrow-bandgap quantum dots (QDs) of different semiconductors and carbon quantum dots (CQDs) [24–28]. To establish a proper channel among the QDs and TiO₂ for effective induced charge separation, heterojunction formation is critical. Despite the incorporation of QDs, photocatalytic activity has not been remarkably improved because of the high instability, rich surface traps, and inevitable photo-oxidization of QDs [29]. Moreover, the use of heavy-metal ions (e.g., Zn, Cu, Cd, and Pb) which are toxic, raises concerns about environmental and human safety [30]. Therefore, the development of an eco-friendly, highly efficient, and recyclable catalyst that can efficiently harvest solar energy and form heterojunctions under suitable conditions is a formidable challenge.

Recently, CQDs have emerged as materials that introduce new possibilities for the development of heterojunctions because of their novel electronic and optical properties with improved photocatalytic activity. As a unique class of CQDs, graphene quantum dots (GQDs) are a nontoxic metal-free zero-dimensional (0D) material usually composed of one or a few layers of graphene and with diameters in the nanometer range [31]. GQDs have a wide range of applications in energy conversion, bio-imaging, drug delivery, sensing, solar energy conversion [32], and light-emitting diodes [33]. Moreover, they exhibit strong fluorescence and semiconducting properties that arise from their pronounced edge effects, quantum confinement, and functionalities [34]. The substantial UV-vis absorption capability of GQDs is provided by the π -plasmon absorption effect [35]. GQDs possess a tunable wide energy bandgap that can be altered by changing the size and functionalities on edge sites [36]. In addition to these merits, pure GQDs have a large exciton binding energy (0.8 eV calculated for 2 nm GQDs), which enhances the recombination rate, resulting in poor catalytic behavior [37]. Doping of different atoms such as nitrogen (N) and sulfur (S) into the lattice of GQDs has been reported to be the most effective approach to modifying the electronic, optical, and transport properties of GQDs to achieve fast electron transfer [38,39]. Shen et al. have reported that coupling of N- and S-GQDs with other materials results in the formation of an advanced hybrid photocatalyst that promotes photocatalysis [40]. Previous reports have indicated that TiO₂ nanoribbons and carbon nanotube composites exhibit faster photocatalytic degradation of methylene blue (MB) than TiO₂ alone [41]. Graphene and titania interfaces as Schottky-like nanocomposites for efficient photocatalysis have been reported [42]. Zhu et al. suggested a self-assembly method for preparing WSe₂-graphene-TiO₂ for dye degradation and hydrogen production [43]. C–O–Ti bond formation has been reported in TiO₂-graphene composites as a result of free-electron interactions [44]. However, to the best of our knowledge, a pathway for different synthesis routes of doped GQDs and forming TiO₂ heterojunctions has not yet been addressed. Thus, we propose an essential mechanism, the simplest method of doping, and oxygen functionalities' role on edge states of GQDs via acid treatment and the formation of GQDs nanocomposite with TiO₂ as a promising stable photocatalyst.

Here, a novel top-down synthesis of N, S co-doped GQDs via simple cutting methods using different one-dimensional carbon nanomaterials (carbon nanotubes (CNT), reflux carbon nanotubes (RCNT) [45,46], and carbon nanofibers (CNF) [47,48]) as precursors is reported. In the present study, we elucidated the comparative behavior of N, S co-doped GQDs and their respective GQDs-TiO₂ nanocomposites, named as (CNT-GQDs-TiO₂, RCNT-GQDs-TiO₂, and CNF-GQDs-TiO₂) as a highly robust visible-light sensitizer with a tunable bandgap, optical, and capacitive parameters. As-prepared GQDs were used to sensitize a TiO₂ photocatalyst for degradation of MB as a model pollutant dye. The mechanism of heterojunction formation between the GQDs and TiO₂ for charge separation at the interface was proposed through MB degradation and cyclic runs of samples to express the

photocatalytic properties of nanocomposites. To elucidate the role of free radicals in the photodegradation of MB, scavenger tests on a complete set of as-prepared nanocomposites were also performed. The degradation pathway, interfacial charge transfer mechanism, and significance of the metal-free carbon nanomaterial-based photocatalyst are discussed.

2. Results and Discussion

2.1. Physiochemical Properties

Figure 1 shows the morphology of GQDs and GQDs-TiO₂ nanocomposites via images captured by FE-TEM and FE-SEM instruments. FE-SEM and FE-TEM image of the CNT-GQDs shows ring formation due to strong sp² bonding of carbon atoms, indicated by a white hexagonal outline of the shape of GQDs exhibit an average diameter of 8 nm. Similarly, FE-TEM images for the RCNT-GQDs and CNF-GQDs shows average diameters of 15 nm and 100 nm, respectively. Particle size of CNT-GQDs varied from 3 to 8 nm and average particle size is approximately 5 nm. Whereas, RCNT-GQDs size range lies between 8 to 20 nm with 13 nm average size and CNF-GQDs size is between 70–120 nm with average size of 90 nm. Agglomeration and overlap phenomena are observed because the high surface-area-to-volume ratio favors large surface energy and instability in the GQDs, especially in the case of CNT-GQDs and RCNT-GQDs [49]. To prepare a nanocomposite in which these effects of GQDs are diminished, we strongly sonicated GQDs and stirred them with TiO₂ to balance the surface energy and stability of the nanocomposites, which also promotes the formation of heterojunctions between the GQDs and TiO₂. Well distributed and firmly decorated GQDs are observed on TiO₂ surface. CNT-GQDs-TiO₂, RCNT-GQDs-TiO₂, and CNF-GQDs-TiO₂ exhibit lattice spacings of 0.2873 nm, 0.3368 nm, and 0.4275 nm corresponding to the (004), (112) and (101) planes, respectively. The FE-TEM images of nanocomposites demonstrate that the GQDs are amorphous phases and the TiO₂ is crystalline phases; these phases are clearly seen, where the GQDs (amorphous) lie on the TiO₂ (crystalline) lattice to form the well-structured nanocomposites.

Pristine phases of the crystal and structural behavior of as-prepared GQDs and GQDs-TiO₂ nanocomposites were characterized by XRD on the basis of Bragg's law, $2d\sin\theta = n\lambda$ ($n = 1$, $\lambda = 0.154$ nm). Detailed XRD patterns of GQDs and GQD-TiO₂ nanocomposites are shown in Figure 2a. Intense peaks of CNFs, CNTs at $2\theta \approx 25^\circ$ and 27.95° are predominant GQDs data (JCPDS-ICDD file No. 75-1621), these peaks represent the (002) and (101) planes of sp²-hybridized hexagonal carbon atoms, respectively [50]. Whereas, crystalline phases of TiO₂ represented by $2\theta \approx 25^\circ$ and 48° corresponding to (110) and (200) planes, respectively and indicating good agreement with the standard spectrum (JCPDS-ICDD file No. 21-1272). Traces of S in the CNF-GQDs with 40% crystallinity and the RSWCNT-GQDs with 22% crystallinity are confirmed by the (220) plane with an interlayer spacing of 0.39 nm. Planes (110) represent oxygen abundance in GQDs. Peaks at $2\theta \approx 24.9^\circ$ and 27.2° correspond to the anatase phase of TiO₂ and the graphitic structure of the GQD-TiO₂ nanocomposite, with *d*-spacings of 0.35 nm and 0.32 nm, respectively [51]. An intense (101) peak represents a high weight percentage of TiO₂ in the prepared nanocomposite as compared with the GQDs. Prominent peaks for GQDs in the XRD of the GQDs-TiO₂ were absent because of the lesser proportion of GQDs and the high surface coverage by TiO₂. We concluded that the GQDs' peaks are obscured by the dominant TiO₂ peaks. Similarly, peaks related to the presence of S and N in the GQDs are also diminished in the patterns of the nanocomposite samples. Additional peaks observed at $2\theta \approx 33.5^\circ$ and 37.4° denote strong C–O–Ti bonding [52]. Because of interface formation and proper dispersion of the GQDs over the TiO₂ surface, the crystallinity of samples appears to increase to approximately 37% for the CNT-GQDs-TiO₂, RCNT-GQDs-TiO₂, and 47% for the CNF-GQDs-TiO₂ but cannot be increased further because of the abundance of O and other impurities.

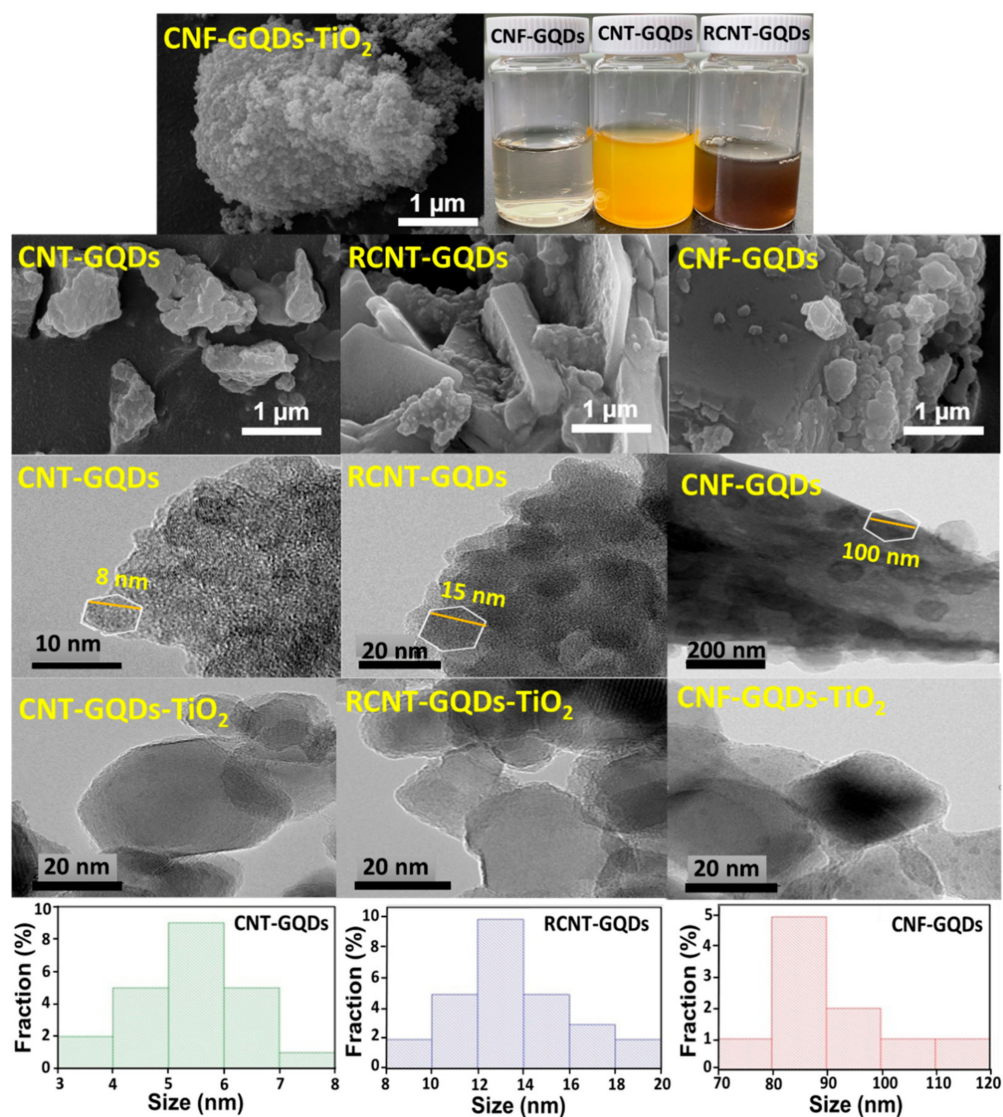


Figure 1. FE-SEM micrographs and FE-TEM images of as-synthesized GQDs with size distribution and their respective GQDs-TiO₂ nanocomposites.

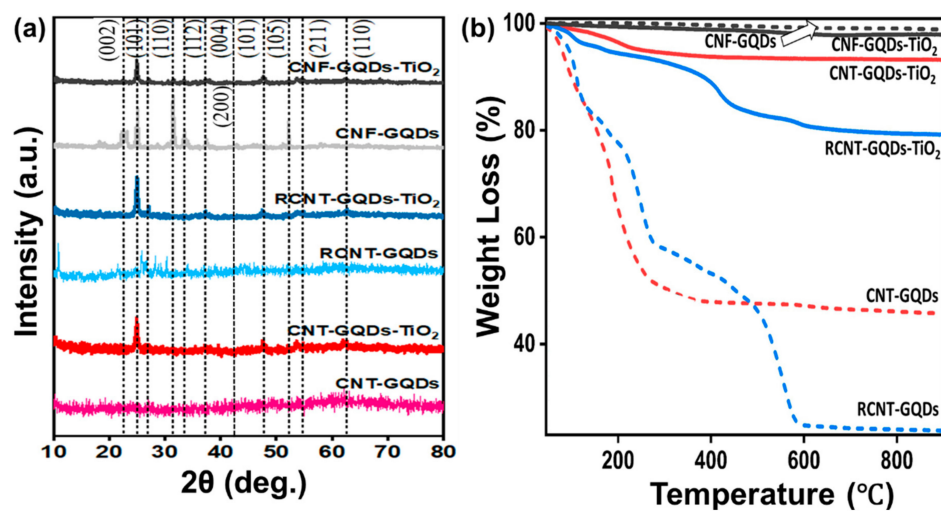


Figure 2. (a) XRD pattern of as-synthesized GQDs and their respective GQDs-TiO₂ nanocomposites. (b) TGA analysis of as-synthesized GQDs and their respective GQDs-TiO₂ nanocomposites.

TGA was carried out on GQDs-TiO₂ nanocomposites to clarify the structural thermal stability, bonding with GQDs, and the significance of the nanocomposite properties. Thermograph temperature in the range of 50–150 °C, 150–350 °C, 350–550 °C, and above 550 °C denote physio-adsorbed water, dehydration–decarboxylation of bonded water and functional groups, oxidation of amorphous groups, and oxidation of graphitic structures, respectively [53]. Figure 2b shows the TGA curve of the GQDs-TiO₂ nanocomposites. Interestingly, these thermographs show nanocomposite formations that denote low weight loss and indicate strong bonding of the GQDs onto the TiO₂ surface. The CNT-GQDs-TiO₂, RCNT-GQDs-TiO₂, and CNF-GQDs-TiO₂ demonstrate 6.81%, 20.81%, and 2.09% mass loss, respectively. These results undoubtedly predict the formation of thermally stable structures of nanocomposites. Minor weight loss in CNF-GQDs-TiO₂ indicates strongest covalent bonding between CNF-GQDs and TiO₂. Specifically, it indicates chemisorption in the investigated temperature range, rearrangement of lattices when in-plane (C–O) functional groups were transferred to oxygen-deficient vacancies in the TiO₂ plane, and the formation of stable C–O–Ti bonds. This explanation reflects the roles of functional groups in GQDs and oxygen vacancies in TiO₂ in determining the configuration of nanocomposites.

The heterostructure interfacial chemical bonding and interaction in GQDs-TiO₂ samples were investigated by XPS analysis. Peaks appeared at binding energies of 531, 284, 406, and 168 eV in the spectra of the GQDs, corresponding to O 1s, C 1s, N 1s, and S 2p, respectively. Identical peaks with a slight change in intensity were observed in the spectrum of the GQDs-TiO₂ nanocomposites, along with an additional peak of Ti 2p at 458 eV, as shown in Figure 3a–c. High-resolution C 1s spectra were fitted with two Gaussian peaks with maxima at 284.28 and 287.48 eV in the spectrum of CNT-GQDs-TiO₂ as shown in Figure 3d, signifying C=C bonds of a graphitic honeycomb structure and other show a Ti–O–C bond peak associated with titanium carbonate and strong C=C peak of GQD, respectively. Deconvoluted C 1s peaks for the spectrum of the RCNT-GQDs-TiO₂ are attributed to titanium carbide and C=C as mentioned in Figure 3e. These results strongly evidence the formation of C–Ti bonds and C–O–Ti bonds. Ti–C bonds exhibit greater stability and better interfacing for RCNT-GQDs-TiO₂ nanocomposite. However, the C 1s peak fitting in Figure 3f results for CNF-GQDs-TiO₂ that are identical to RCNT-GQDs-TiO₂, which indicates C–Ti and C–O–Ti bond formation. C 1s range of GQDs-TiO₂, C=C bond formation indicates that the synthesis of nanocomposites using high sonication of GQDs and extended stirring times at a certain temperature led to a well-decorated GQDs-TiO₂ interface with strong bonding between Ti–O and Ti–O–C.

Meanwhile, a core-level study of the high-resolution O 1s spectra of the GQDs-TiO₂ nanocomposites as shown in Figure 3g–i revealed relevant peaks centered at 529.18, 530.6, and 532.08 eV, which are attributed to Ti–O–Ti, C=O, and Ti–O–C interfacial bonds, respectively [54]. The Ti–O–Ti bond peaks are prominent because the TiO₂ content of nanocomposites was much greater than their GQD and O^{2−} contents. After analyzing the spectroscopic data, it can be concluded that reaction parameters such as temperature, chemical treatment, and time cause changes in the ratio of N, S- heteroatom doping extent, oxygen functionalities, and physiochemical properties of as-prepared GQDs that affects overall bonding strength of the nanocomposites. N and S heteroatom dopant traces can be clearly seen in CNF-GQDs-TiO₂ XPS data, whereas absence or negligence of S doping in CNT-GQDs-TiO₂ and N doping in RCNT-GQDs-TiO₂ were observed. Due to which it can be stated that CNF-GQDs-TiO₂ can experience the synergistic effect that leads to the better performance of nanocomposite because of strong absorption capability and photosensitizer ability, as discussed in the next sections. These XPS results are fully consistent with the XRD analyses.

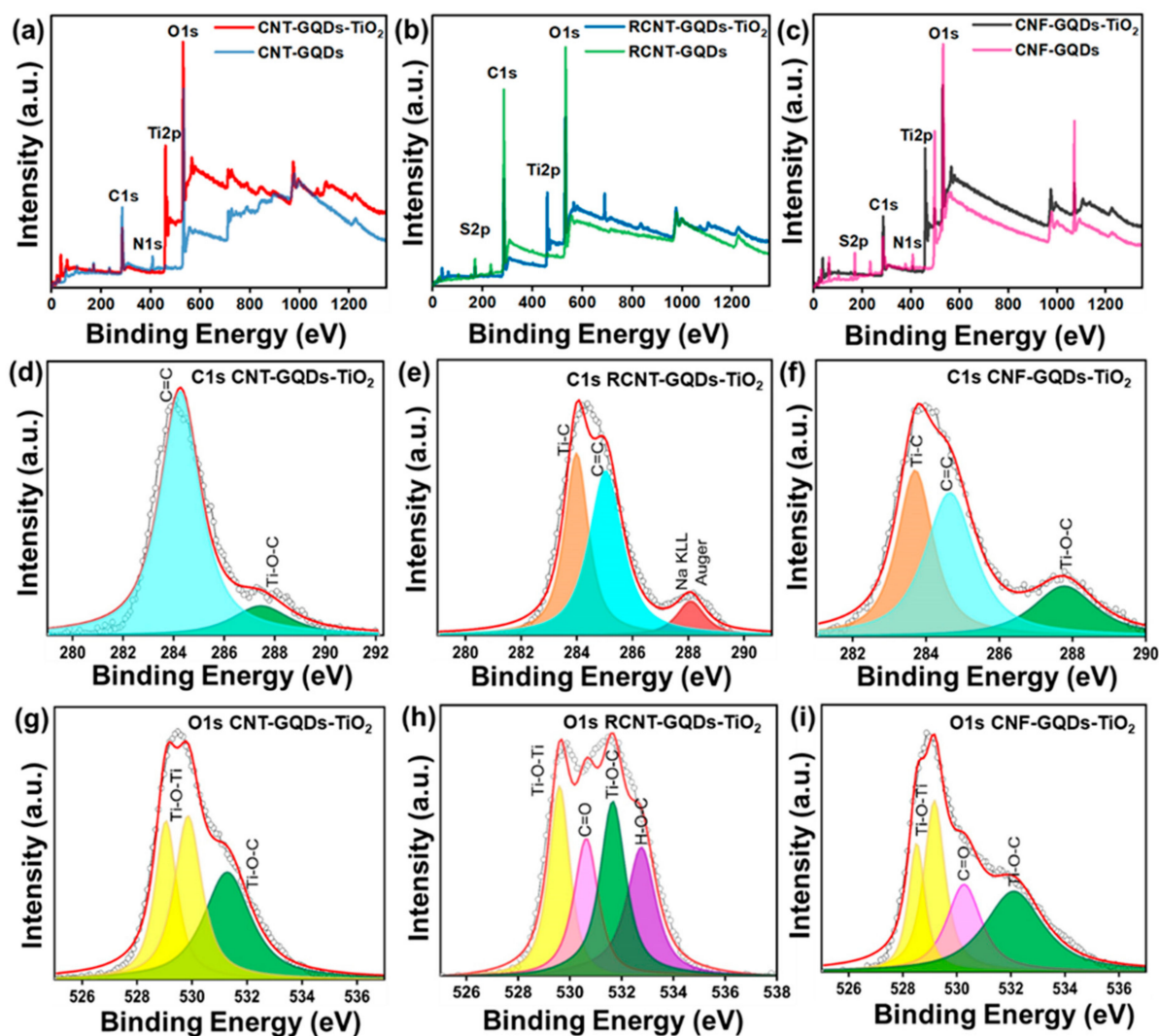


Figure 3. Synoptic XPS survey scan of (a) CNT-GQDs and CNT-GQDs-TiO₂ nanocomposites, (b) RCNT-GQDs and RCNT-GQDs-TiO₂ nanocomposites, (c) CNF-GQDs and CNF-GQDs-TiO₂ nanocomposites. High resolution XPS spectra of C1s peak (d) CNT-GQDs-TiO₂, (e) RCNT-GQDs-TiO₂, (f) CNF-GQDs-TiO₂. High resolution XPS spectra of O1s peak (g) CNT-GQDs-TiO₂, (h) RCNT-GQDs-TiO₂, (i) CNF-GQDs-TiO₂.

2.2. Optical Study and Photoelectrochemical Study

Figure 4a shows the UV-Vis absorption spectra for GQDs-TiO₂ nanocomposites. Figure 4c inset represents a UV-Vis plot of the GQD absorption spectra. All the GQDs show characteristic π - π^* transitions below 300 nm within the sp^2 C=C hybridized framework of carbon domains [55]. The absorption tail extending to ~350 nm in the visible region was assigned to the $n \rightarrow \pi^*$ transitions of nonbonding electrons of O, N, and S atoms [56]. Greater absorption, specifically in the case of CNF-GQDs, was due to these extra electrons caused by N, S doping. PL spectra of as-prepared GQDs samples tested in powder form by excitation of a He-Cd laser at 325 nm. For better understanding of GQDs band gap, Tauc plot of respective GQDs was shown in Figure 4c. Bandgap corresponding to CNT-GQDs, RCNT-GQDs, and CNF-GQDs as obtained by the formulation, were 3.3, 2.2, and 2.8 eV, respectively. For composites tailored band gap, Tauc plot of respective GQDs-TiO₂ nanocomposites was shown in Figure 4b. The bandgap of the samples can be easily determined by the intersection point of the energy axis with the slope of the curve in graph. Bandgap corresponding to CNT-GQDs-TiO₂, RCNT-GQDs-TiO₂, and CNF-GQDs-TiO₂ nanocomposites as obtained by the formulation, were 2.21, 2.23, and 2.29 eV,

respectively. Ti–O–C interfacial bond formation and intimate interaction in nanocomposites could decrease the bandgap value of nanocomposites. Interaction between TiO₂ and GQDs was because of chemical coupling and influence of C atoms on the molecular orbitals of TiO₂, as a result, the bottom band of the nanocomposite lowers itself as compared with that of TiO₂. Incorporation of GQDs will enhance the lifetime of electron-hole pairs and result in faster photogenerated electron transfer in TiO₂ due to π -conjugation of the GQDs.

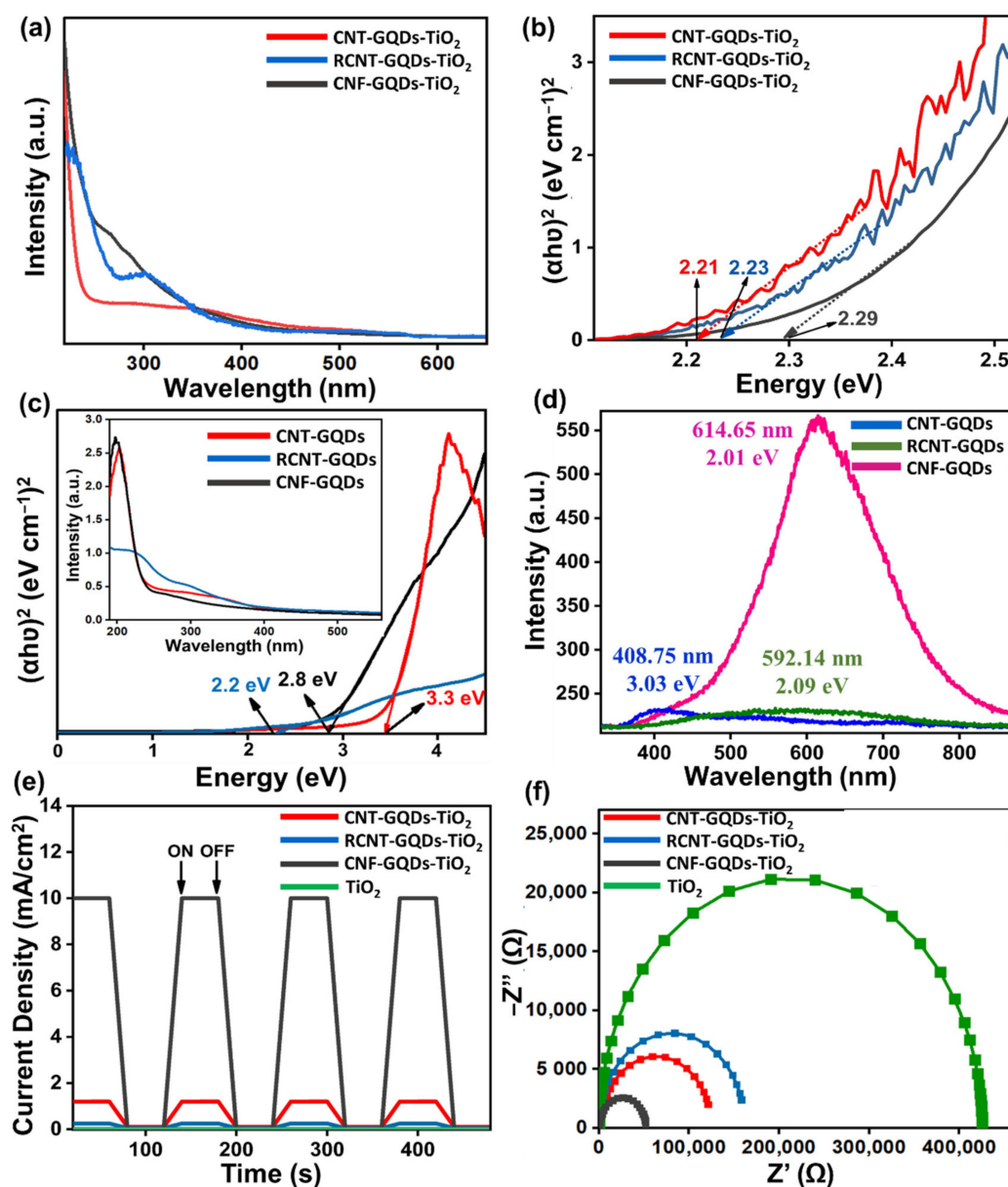


Figure 4. (a) UV-vis absorption of as-synthesized GQDs-TiO₂ nanocomposites, (b) Tauc plot of respective GQDs-TiO₂ nanocomposites, (c) Tauc plot of as-synthesized GQDs with respective UV-vis absorption as inset image, (d) Photoluminescence (PL) spectra of as-synthesized GQDs excited at 325 nm by He-Ne laser. Photoelectrochemical analysis (e) Transient photocurrent response of the as-prepared GQDs-TiO₂ nanocomposites, (f) EIS measurements.

Figure 4d depicts the photoluminescence (PL) spectra of three GQDs, CNF-GQDs clearly show the strongest PL emission in the orange-red region of the visible spectra, with a bandgap energy of 2.01 eV; similarly, the RCNT-GQDs emit in the yellow-orange region, with an equivalent range of photon energy of 2.09 eV but with lesser intensity than the emission of the CNF-GQDs. By contrast, the CNT-GQDs exhibit totally different PL

emission at 408.75 nm with a 3.03 eV bandgap energy in the violet region but with the same intensity as the emission of the RCNT-GQDs. PL phenomena were observed in GQDs when the excitation wavelength was comparable to the transition wavelength. Long wavelengths were absorbed and emitted by C=S and C=N chromophores, which resulted in red-yellow emission; by contrast, $n \rightarrow \pi^*$ excitation of C=O chromophores were assigned to short wavelengths with violet and blue emission [57].

Table 1 denotes the atomic % of elements clearly shows that the CNF-GQDs and RCNT-GQDs were rich in S-group content, whereas the CNT GQDs were rich N-group content. Because of the abundance of S groups and some traces of N in conjugated molecules of CNF-GQDs, the $n \rightarrow \pi^*$ transition of the C=S group dominates with overlapping of N and O groups in CF-GQDs [58], which led to the synergistic effect of these three groups in lattice formation, as confirmed from the XRD and XPS analysis. Hence, orange-red emission was observed upon excitation of CNF-GQDs. The proposed mechanism responsible for the CNF-GQDs strong PL emission is S π^* orbital insertion between C n and N π^* orbitals and the formation of a low-electronegative S state. Remarkable difference in PL intensities of GQDs strongly justifies the CNF-GQDs efficiency, these property variations experienced by GQDs was based on synthesis method. On comparing the key parameters of synthesis process, we conclude that simple oxidative cutting with comparatively low temperature range (110–120 °C) using CNF is more feasible and effective for GQDs synthesis because refluxing process and followed hydrothermal reaction at high temperature range proved to be harsh on the surface and also it distorts the edges and structure of the GQDs which hinders the oxygen vacancies, graphitic properties and anchoring properties those can be inherited by GQDs from CNTs. This proves the CNF-GQDs with higher PL intensity as a potential contender for photocatalytic process.

Table 1. Atomic percentage analysis with statistical error using XPS spectrometer for as-prepared GQDs and GQDs-TiO₂ nanocomposites.

Elements	CNT-GQDs	CNT-GQDs-TiO ₂	RCNT-GQDs	RCNT-GQDs-TiO ₂	CNF-GQDs	CNF-GQDs-TiO ₂
Atomic percentage						
C	44.14 ± 2.0	27.41 ± 0.2	62.51 ± 3.2	51.07 ± 5.2	24.51 ± 0.7	37.76 ± 4.7
O	47.61 ± 1.0	53.11 ± 1.0	33.51 ± 3.5	38.11 ± 8.5	62.99 ± 4.1	44.55 ± 0.7
N	6.53 ± 0.8	2.45 ± 0.5	0.21 ± 0.1	0.12 ± 0.5	4.55 ± 2.9	1.46 ± 0.9
S	1.72 ± 0.1	0.15 ± 0.04	3.69 ± 0.09	2.52 ± 0.6	7.95 ± 0.4	1.75 ± 0.3
Ti	-	17.22 ± 0.08	-	8.19 ± 2.2	-	14.49 ± 2.6

Separation of photogenerated charge carriers of as-synthesized GQDs-TiO₂ nanocomposites can be investigated by photoelectrochemical study at room temperature using an Ivium electrochemical workstation under solar simulator. The electrolyte used through the experiments was 2 M KOH aqueous solution. A typical three-electrode setup consisting of a working electrode, a Pt coil as a counter electrode, and a saturated calomel electrode (SCE) as the reference electrode was used. Fluorine doped tin oxide coated (FTO) glass electrode was prepared by spin coating technique at 20,000 rpm for 10 s in three runs with exposed area of 1 × 1 cm². Coating slurry was prepared by dispersing 5 mg of photocatalyst in 1 mL ethanol containing 10 µL Nafion. Electrodes were oven dried for 3 h and calcinated at 200 °C in nitrogen atmosphere for 2 h to augment adhesion.

Photoelectrochemical analysis of GQDs-TiO₂ nanocomposites as shown in Figure 4e,f transient photocurrent and EIS graphs respectively. While referring to transient current curves, it can be clearly observed that TiO₂ has negligible current response as compared to prepared nanocomposites. CNT-GQDs-TiO₂ and RCNT-GQDs-TiO₂ electrodes exhibit high photocurrent density, well stable and longstanding photoresponse under visible light projection. CNF-GQDs-TiO₂ electrode produces much larger photocurrent density than other electrodes, this indicates that CNF-GQDs-TiO₂ possess highest charge transfer rate and improved photogenerated charge carriers' separation efficiency. Meanwhile, more effective way to reveal electron transfer efficiency of as prepared sample electrodes is

through EIS (electrochemical impedance spectroscopy). In Figure 4f, clear comparative analysis can be done among the nanocomposites based on EIS curve radius. Shorter the radius implies better mobility and well separated photogenerated charge carriers. CNF-GQDs-TiO₂ demonstrates the smallest radius curve among all, results in better charge transfer at electrode interface that enhance the separation of carriers. These electrochemical results prove that the GQDs-TiO₂ heterojunctions specially CNF-GQDs-TiO₂ serves as electron harvester for improved degradation performance and separation of charge carriers, this phenomenon can be thoroughly observed in next sections.

2.3. Visible-Light Photocatalysis and Mechanism Studies

Figure 5 presents the visible-light photocatalytic degradation kinetics for different nanocomposites samples toward the degradation of MB as a model pollutant dye. Figure 5a shows the photocatalytic degradation behavior of different compositions of GQDs-TiO₂ nanocomposites. MB degradation first-order-rate-constant behavior was fitted using the Langmuir-Hinshelwood rate formalism, which represents the kinetics of photocatalytic reaction in different catalysts and was expressed as $\ln(C/C_0) = k_a t$, where k_a is the pseudo-first-order-reaction rate constant and C and C_0 denote the MB concentrations after and before irradiation time t , respectively [59]. The rate constant for different catalysts was obtained from the slope of the straight-line plot shown in Figure 5b. All the as-prepared nanocomposites exhibit an excellent degradation percentage, as shown in Figure 5e. The CNT-GQDs-TiO₂ sample showed a dramatic increase in degradation percentage to 99.78% in 90 min; similar results were obtained with the RCNT-GQDs-TiO₂ and CNF-GQDs-TiO₂ nanocomposites. Meanwhile, CNF-GQDs-TiO₂ exhibited the fastest degradation kinetics, with 99.39% degradation in 60 min of light irradiation. Graphical representation of the rate constants for different nanocomposites is shown in Figure 5f. These data for samples show that GQDs-TiO₂ exhibit an approximately 2.3 to 3-fold higher degradation rate constant than the commercial P25 photocatalyst. The highest rate constant recorded for the CNT-GQDs-TiO₂ was $6.75 \times 10^{-2} \text{ min}^{-1}$, whereas that of the TiO₂ was $2.48 \times 10^{-2} \text{ min}^{-1}$. The characteristic absorption peak of MB rapidly decreased in intensity in the experiments with all of the prepared nanocomposites; also, this decrease to a certain level was also obtained with TiO₂ (79% degradation). As-prepared GQDs show strong optical absorption capabilities in a wide light spectrum but with poor photocatalytic properties ascribed to their corresponding large binding energy. The key role of a stable heterojunction interface is evident when the GQDs and TiO₂ are blended with each other to form an optimum nanoscale composition containing well-dispersed soluble GQDs on the surface of TiO₂ nanoparticles using a simple sonication and stirring method. The content of GQDs cannot be increased further because of their strong tendency to aggregate on the TiO₂ surface, which retards the photocatalytic process remarkably. The construction of well-dispersed nanoparticle heterojunctions is critical and can be effectively achieved through bandgap narrowing, as shown by the Tauc plot previously. By contrast, C–O–Ti bond formation ascribed to chemisorption of GQDs on the TiO₂ surface plays a strong role in strengthening the interaction between nanocomposites [60]. This strong coupling of GQDs with TiO₂ forms the hot-carrier injection pathway, whereas N and S doping causes substantial bandgap reduction. Because of this heterojunction formation, efficient charge separation occurred on the surface, results in a higher photodegradation rate. Comparatively slight variation among the degradation rates of the samples was observed because of the difference in the bandgap value of nanocomposites, where the smallest bandgap value was reported for CNT-GQDs-TiO₂, which exhibited the highest degradation rate of 99.78%, confirming that the bandgap is an essential factor in dye degradation. CNT-GQDs-TiO₂ exhibits slightly higher degradation from CNF-GQDs-TiO₂ because of its smaller bandgap as it can be seen in Tauc plot, but based on TGA analysis and repetitive cyclic runs, it is not as stable as CNF-GQDs-TiO₂. Therefore, CNF-GQDs-TiO₂ is considered as the best suited composite among all due to strong covalent bonding between CNF-GQDs and TiO₂ that indicates stable C–O–Ti bonds formation. Also, CNF-GQDs experienced the N and S

dopant synergistic effect that results in better performance of nanocomposite with strong absorption capability and photosensitizer ability.

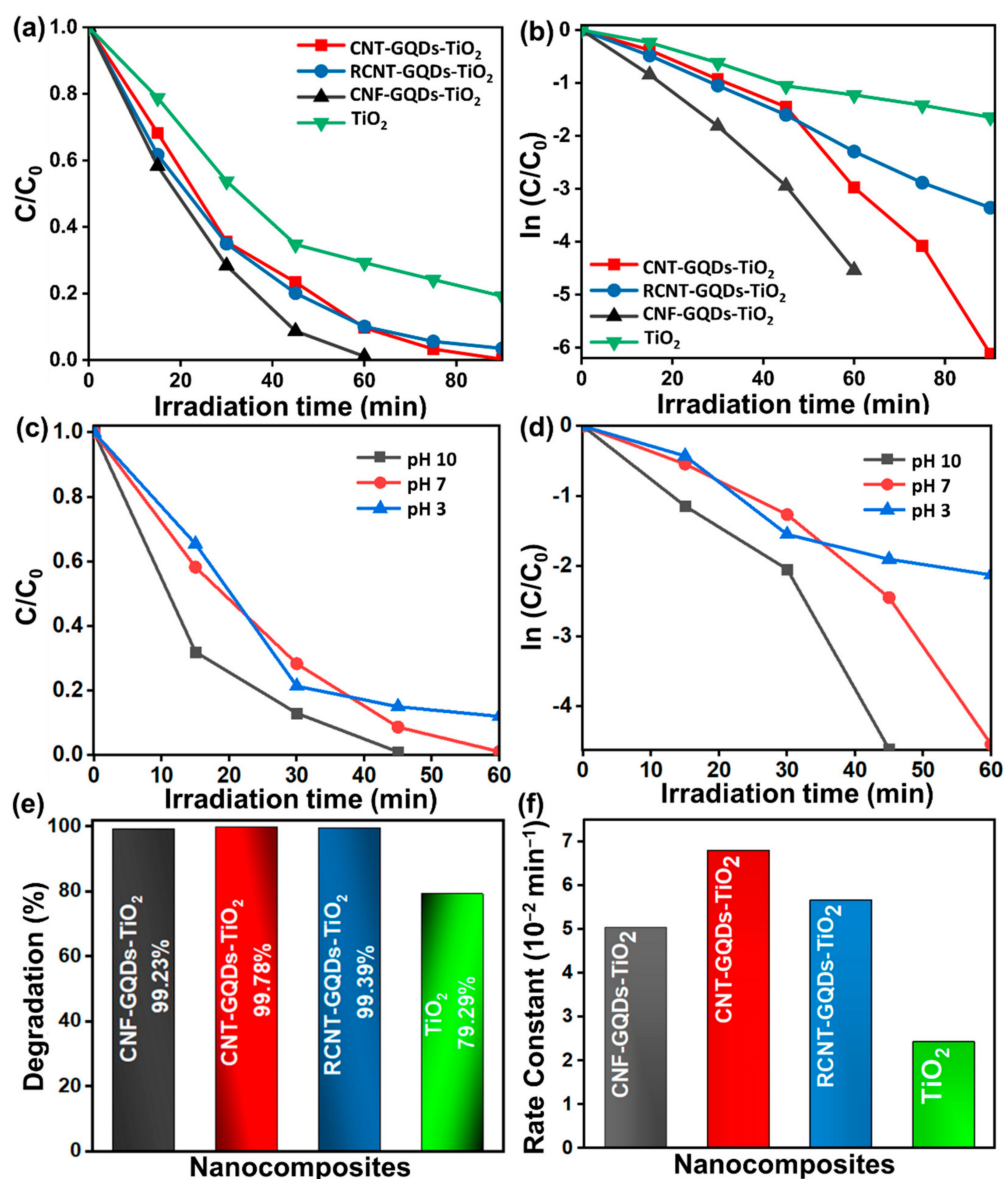


Figure 5. Visible light photocatalytic degradation of MB for as-synthesized GQDs-TiO₂ nanocomposites (a) Change in relative concentration (C/C_0) of MB in GQDs-TiO₂ nanocomposites as a function of irradiation time up to 90 min, (b) Derived plot from same data to study $\ln(C/C_0)$ variations with irradiation time. pH variation effect on the (c) Change in relative concentration (C/C_0) as a function of irradiation time up to 60 min using CNF-GQDs-TiO₂ nanocomposites, (d) Respective derived plot of $\ln(C/C_0)$ variations with irradiation time. (e) Comparison of MB degradation in different nanocomposites, (f) Comparative study of first order rate constants of as-prepared GQDs-TiO₂ nanocomposites.

pH effect is an important parameter for the dye degradation. MB degradation was tested in the pH range between 3 to 10, pH values were adjusted using H₂SO₄ and 0.1 mol/L NaOH. Experimental condition was identical as mentioned in the experimental section. Figure 5c,d shows that photodegradation rate was improved by increasing the pH values. At pH 3, degradation efficiency was dropped to 84%. At pH 10 and pH 7, degradation efficiency is same ~99.23% but with the increase of pH value the process of degradation become fast. At pH 10, 99.23% degradation was achieved in 45 min. This shows that

alkaline conditions increase the reaction rate due to the abundance of hydroxyl ions that helps in increasing the degradation reaction. Whereas at low pH, reaction rate reduced due to excess of H^+ ions [61]. Hence, it can be stated that alkaline medium is favorable for MB degradation using CNF-GQDs-TiO₂ nanocomposites.

GQDs-TiO₂ composites were studied by many groups with TiO₂ nanostructures (nanotubes, nanoparticles, and nanosheets) for the degradation of organic dyes to find the best suited one as shown in Table 2. Various chemical composition and formation methods were used to synthesize GQDs and composites with desired physiochemical properties that results in fastest, stable, and complete organic dye degradation. GQDs, N-GQDs, and N, S-GQDs based TiO₂ composites were studied previously but results in slow and lesser degradation efficiency [62–64]. Whereas, Tian et al. synthesized the N, S-GQDs based reduced graphene oxide (rGO)-TiO₂ nanotubes (NTs) using hydrothermal and stirring process for degradation methyl orange (MO). This results in MO degradation in 4 h upto 90% [65]. This work, have presented the three types of GQDs formation with different N, S doping amount due to the different precursors and process of synthesis. Best results were obtained by TiO₂ composites formed using CNF-GQDs due to strong covalent bonding between CNF-GQDs and TiO₂ defining its stability, also it indicates chemisorption and rearrangement of lattices when in-plane (C-O) functional groups were transferred to oxygen-deficient vacancies in the TiO₂ plane to form stable C–O–Ti bonds. This reflects the role of functional groups in GQDs and oxygen vacancies in TiO₂ for determining the configuration of nanocomposites. CNF-GQDs experienced the N and S dopant synergistic effect that leads to the better performance of nanocomposite with strong absorption capability and photosensitizer ability. Based on this, we concluded that CNF-GQDs-TiO₂ has shown the fastest degradation (60 min) of methylene blue (MB) with highest efficiency of 99.23% as compared with the previously reported articles.

Table 2. Comparative data analysis of dye degradation using GQDs based TiO₂ nanocomposites.

Photocatalyst	Pollutant	Irradiation Time (min)	Degradation Efficiency (%)	References
GQD/a-TiO ₂	Rhodamine B	35	97	[62]
GQDs/TiO ₂	Methylene Blue	120	96.70	[63]
GQDs/TiO ₂	Rhodamine B	60	70	[66]
3DGA@CDs-TNs	Rhodamine B	60	97.60	[67]
N-GQDs/TiO ₂	Rhodamine B	120	94	[64]
N-GDQs/TiO ₂	Methylene Blue	150	100	[68]
N-GDQs/TiO ₂	Methylene Blue	70	85	[69]
Ti ³⁺ -TiO ₂ /GQD NSs	Methylene Blue	60	90	[70]
NSTG	Methylene Blue	240	98.40	[40]
N, S-GQDs/rGO/TiO ₂ NT	Methyl orange	240	90	[65]
TiO ₂ /rGO	Methylene Blue	120	91.48	[71]
CNF-GQDs-TiO ₂	Methylene Blue	60	99.23	This work

Another essential factor for photocatalysts is reusability and stability. The reusability of the nanocomposites was tested over three repeated cyclic runs of photocatalysis, as shown in Figure 6a. These stability results provide important facts about catalysts. After three cyclic runs, the CNT-GQDs-TiO₂ demonstrated a 0.54% decrement. By contrast, the RCNT-GQDs-TiO₂ exhibited only 55.5% degradation, with a 44.11% decrement compared with its initial degradation results. The CNF-GQDs-TiO₂ catalyst was the most stable for three repeated cyclic runs. Reason behind CNF-GQDs reusability and long-term stability was N, S doping, thermally stable structure and oxygen mediated vacancies which was responsible for C–O–Ti bonding. Poor stability of the RCNT-GQDs-TiO₂ and strong bonding of the CNF-GQDs-TiO₂ were confirmed by the TGA results.

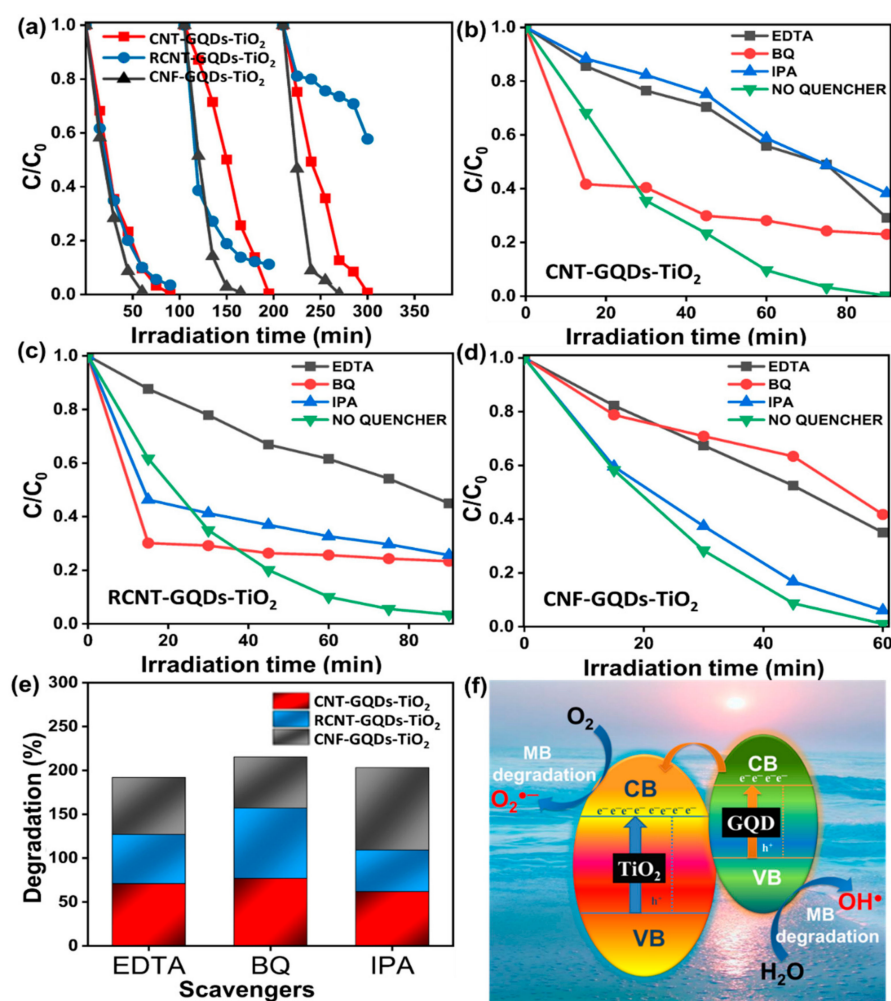


Figure 6. (a) Cyclic runs of MB degradation under visible light exposure for GQDs-TiO₂ nanocomposites. MB degradation concentration in absence and presence of different scavengers (scavengers: IPA~•OH, BQ~O₂^{•-}, EDTA~h⁺) by (b) CNT-GQDs-TiO₂, (c) RCNT-GQDs-TiO₂, (d) CNF-GQDs-TiO₂. (e) Comparative analysis of effect of scavengers on MB degradation. (f) Schematic illustration of free radical generation and interfacial charge separation at GQDs-TiO₂ nanocomposite junction for MB degradation.

To investigate the role of the electron, transfer mechanism and the reaction process in a typical photocatalysis system, active species such as holes (h⁺), hydroxyl radicals (•OH), and superoxide radicals (O₂^{•-}) were studied. Solutions of IPA, BQ, and EDTA scavengers were used to study the roles of •OH, O₂^{•-}, and h⁺, respectively [72]. To investigate and explore their contribution in visible-light photocatalysis, a series of scavenger tests were performed on CNT-GQDs-TiO₂ nanocomposites. The dosage addition of scavengers inhibits the degradation efficiency of MB to various degrees, which refers to the involvement of all oxidative species in the photodegradation system. Changes in relative concentration of MB in different scavengers for all of the as-prepared nanocomposite systems are shown in Figure 6b–d. In the case of IPA addition, the MB was degraded by 61.74% for CNT-GQDs-TiO₂, implying the vital role of •OH radical, and RCNT-GQDs-TiO₂ was quenched to 47.55% in EDTA, indicating the important of h⁺ species in the degradation process. When BQ was added to the CNF-GQDs-TiO₂ system, 58.26% MB degradation was observed, indicating that the major reactive species involved in the process was O₂^{•-}. Figure 6e shows a comparative analysis of the nanocomposite systems with and without scavenger addition and respective values can be seen in Table 3. All studies of samples show the highest quenching of MB degradation in different scavengers. These results indicate that

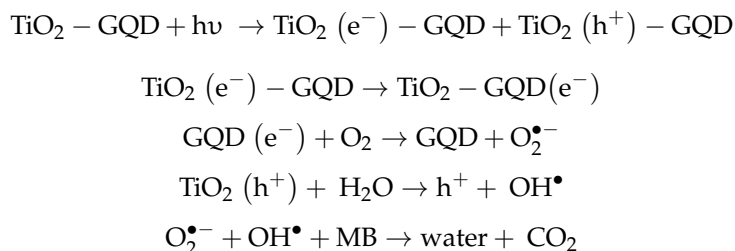
•OH, O₂^{•−}, and h⁺ are the major reactive species in MB degradation for CNT-GQDs-TiO₂, CNF-GQDs-TiO₂, and RCNT-GQDs-TiO₂, respectively.

Table 3. Role of quenchers in UV-Vis photocatalysis of MB degradation.

Quencher	CNT-GQDs-TiO ₂ (% Degradation)	RCNT-GQDs-TiO ₂ (% Degradation)	CNF-GQDs-TiO ₂ (% Degradation)
EDTA	70.89	47.55	64.97
IPA	61.74	56.17	93.94
BQ	76.98	80.15	58.26

Based on the aforementioned results, the degradation mechanism can occur through various steps, implying direct electron transfer. Figure 6f shows the proposed mechanism of free radicals involved in the photodegradation process. The phenomena that lead to the formation of the Schottky barrier between photoexcited electrons in GQDs and the TiO₂ lattice are thermionic emission and quantum tunneling. Achieving thermionic emission was difficult because the complete experimental procedure was carried out at room temperature. Hence, the most likely factor behind electron transport in the GQD–TiO₂ composite was quantum tunneling, which forms the heterojunction type II band alignment.

Degraded methylene blue (MB) results in some intermediate volatile end products of MB solution. When N-S heterocyclic compound of methylene blue was separated 2-Amino-5-dimethylamino-benzenesulfonic acid anion was formed. Degradation intermediate of 2-Amino-5-dimethylamino-benzenesulfonic acid was 4-Amino-benzenesulfonic acid and 2-Amino-5-hydroxy-benzenesulfonic acid. Oxidization of 4-Amino-benzenesulfonic acid results in 4-Nitro-benzenesulfonic acid anion. Products formed after hydroxyl radical attack on the N–S heterocyclic of MB molecules were Dimethyl-(4-nitro-phenyl)-amine and p-Dihydroxybenzene. Tiny molecular products of degradation correspond to succinic acid generated by open-loop benzene [73]. On the basis of these intermediate products, we can deduce the degradation pathway of MB. The photogenerated electrons in the TiO₂ with the in situ excited electrons of GQDs reacts with free radicals. Hence, electrons from the GQDs transfer to the conduction band of TiO₂ to trap the oxygen (O₂) molecule to generate the O₂^{•−} radicals, and h⁺ react with an electron donor (water molecules or hydroxide ions) to yield oxidizing hydroxyl •OH radicals. These generated radicals of O₂^{•−} and •OH are the essential substances to decompose the dye molecules into CO₂ and H₂O. Thus, GQDs with high electron mobility are a perfect electron-transfer tank for enhanced electron–hole separation at the interface of TiO₂. The high degradation of MB in several scavengers can be interpreted as the conversion of O₂^{•−} radical to •OH radical. The possible pathways for MB degradation are expressed by the following reactions:



3. Materials and Experimental

3.1. Chemicals

Vapor-grown carbon nanofibers were purchased from Carbon Nano-material Technology. Co. Ltd., Pohang, Korea. Single-walled carbon nanotubes (SWCNTs (75%)) with an average diameter of 1.8 ± 0.4 nm and length greater than 5 μm were supplied by TuballTM-OCSiAl Pvt. Ltd., Incheon, Korea. TiO₂ powder, sulfuric acid (99.99%), nitric acid (ACS reagent, 70%), methylene blue (MB), 2,3-dichloro-5,6-dicyano-*p*-benzoquinone (98%-BQ), ethylenediaminetetraacetic acid (EDTA, >98%), and isopropyl alcohol solution (70% in

H₂O–IPA) were purchased from Sigma-Aldrich Inc., Seoul, Korea. All reagents were of analytical grade and were used without further purification. Distilled water (18.2 MΩ·cm) was used throughout the experiments.

3.2. Synthesis of GQDs from CNT (CNT-GQDs)

A hydrothermal etching method was used to prepare oxygen-rich GQDs with some traces of N. A total of 300 mg of SWCNTs was refluxed with 150 mL of HNO₃ for 12 h at 100 °C [49]. The suspension was then cooled and filtered to remove the supernatant. The collected residue was dispersed in 50 mL of DI water and heated hydrothermally in a Teflon-lined autoclave at 200 °C for 12 h. The same etching procedure (i.e., refluxing with HNO₃, followed by filtering and hydrothermal heating) was subsequently repeated. After two cycles of the etching process, nitrogen-doped GQDs named as CNT-GQDs were obtained for further use.

3.3. Synthesis of GQDs from RCNT (RCNT-GQDs)

300 mg of SWCNTs was refluxed with H₂SO₄ and HNO₃ (3:1) for 24 h at 120 °C. The mixture was then cooled and diluted with DI water (1:5) while maintaining the pH at ~7. Stepwise gradual heating (100 °C, 150 °C, and 200 °C) of the suspension was conducted at 4 h intervals to obtain sulfur-doped GQDs named as RCNT-GQDs. The as-prepared sample of GQDs was washed with DI water using the filtration technique.

3.4. Synthesis of GQDs from CNF (CNF-GQDs)

Oxygen-rich GQDs doped with nitrogen (N) and sulfur (S) atoms were synthesized using a simple oxidative cutting method. A total of 900 mg of CFs was treated with a mixture of conc. H₂SO₄ and HNO₃ (3:1) under continuous stirring for 24 h at 120 °C. The mixture was diluted with DI water (1:5) after being cooled to room temperature. To maintain the acidity of the mixture, its pH was adjusted to ~7 using NaOH. Finally, a dialysis process of the end product was conducted in a dialysis bag for 3 days and the dialyzed solution was heated at 80 °C to obtain CNF-GQDs.

3.5. Synthesis of TiO₂ and GQD Composite

Different as-prepared samples of GQDs (2 mg/mL) were dispersed in DI water to obtain a uniform suspension using the ultrasonication method. A total of 200 mg of TiO₂ was added to 50 mL of GQD suspension and stirred at 60 °C for 10–12 h, until it dries completely and turned into powder. The GQDs-TiO₂ nanocomposite was obtained in powder form. The nanocomposite samples were named CNT-GQDs-TiO₂, RCNT-GQDs-TiO₂, and CNF-GQDs-TiO₂. The synthesis scheme for respective GQDs is shown in Figure 7.

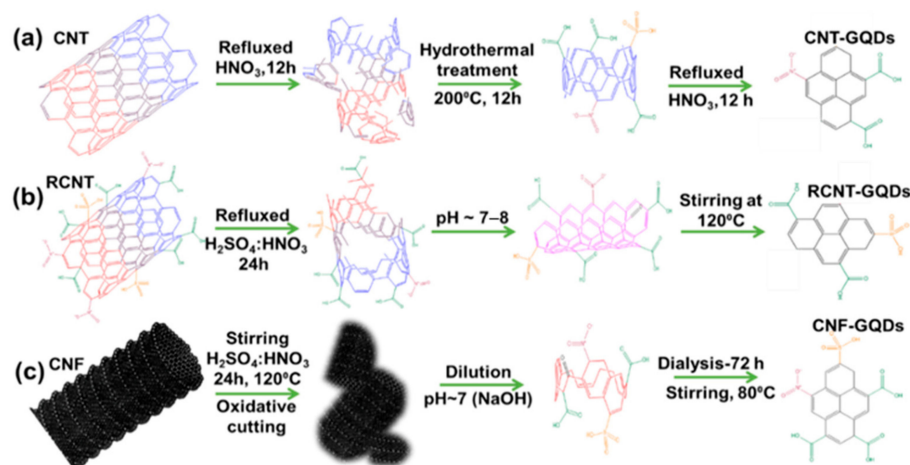


Figure 7. Schematic for the synthesis of N, S co-doped GQDs named as (a) CNT-GQDs, (b) RCNT-GQDs, (c) CNF-GQDs.

3.6. Characterization Techniques

The structure, crystal facets, and phase of the as-prepared samples were examined by powder X-ray diffraction (XRD, Bruker D2 PHASER, Gyeonggi-do, Korea). The morphological features, crystallinity, and chemical composition were studied by field-emission scanning electron microscopy (FE-SEM, Hitachi High-Tech Korea Co., Ltd., S-4300, Seoul, Korea), field-emission transmission electron microscopy (FE-TEM JEM-2100F/JEOL, Seoul, Korea), and energy-dispersive X-ray spectroscopy (EDX) composition analysis. The X-ray photoelectron spectroscopy data were also obtained (XPS, VG Scientific Co., ESCA LAB MK-II, Korea) using a monochromatic Al K α X-ray beam with a current of 20 mA. Quantitative analysis of the solid organic elements present in the samples was performed with an elemental analyzer (Thermo Fisher Scientific, Inc. EA1112, Korea). The specific surface area measurements were performed using an adsorption analyzer (BEL BELSORP, Inc. Japan), and thermogravimetric analysis (TGA, NETZSCH, TG 209 F3, Germany) was carried out for the as-prepared samples at a heating rate of 10 °C/min and with N₂ gas as a purge gas. Photoluminescence (PL) emission spectra were acquired under excitation at 325 nm (RAM Boss, Maple Dongwoo Optron). The UV-vis absorption was performed using a commercial UV-vis spectrophotometer (Scinco, S-3100, Seoul, Korea). Electrochemical analysis was carried out using an Ivium electrochemical analyzer.

3.7. Photodegradation Test

Photocatalytic studies of the GQDs-TiO₂ nanocomposites were conducted using a solar simulator (SUN 2000, Abet Technologies, Inc. Gyeonggi-do, Korea) fitted with a 440 nm cutoff filter. The photocatalytic experiments were carried out in the presence of MB as an organic dye pollutant. A total of 20 mg of catalyst were dispersed in 50 mL of MB aqueous solution with an initial concentration of 10 mg/L. Prior to irradiation, the as-prepared solution was stirred continuously in the dark for 1 h at room temperature to achieve adsorption-desorption equilibrium. At 15 min irradiation intervals, a 5 mL aliquot was withdrawn and analyzed via UV-vis spectrophotometry with a maximum absorption peak at 665 nm.

3.8. Free-Radical Scavenger Test

A free-radical scavenger experiment was conducted to study the involvement of reactive species in the photodegradation of MB. Isopropyl alcohol (IPA) solution, BQ, and EDTA were used as scavengers to analyze the influence of hydroxyl radicals (\bullet OH), superoxide radicals (O₂ \bullet^-), and holes (h⁺), respectively. In the scavenging experiments, 10 mg of a scavenger was mixed with the dye-catalyst solution (20 mg, 10 mg/L). Afterward, the same procedure mentioned in previous section was conducted under identical conditions.

4. Conclusions

A novel approach for the synthesis of N, S doped GQDs from 1-D carbon nanomaterial with high photocatalytic and photoelectrochemical response was suggested. The mechanism of interfacial charge transfer in GQDs-TiO₂ heterojunction is elucidated through the possible C–O–Ti bonds formation. TGA and XPS analyses revealed that N and S doping with in-plane functional groups of GQDs were responsible for stable interface formation between GQDs and TiO₂. Photoelectrochemical measurements provide insights into photocurrent and impedance characteristics of as-prepared GQDs-TiO₂ nanocomposites. Remarkably high degradation percentages of MB under visible-light illumination were observed for CNT-GQDs-TiO₂ (99.78%), RCNT-GQDs-TiO₂ (99.39%), and CNF-GQDs-TiO₂ (99.23%) nanocomposites. Rapid interfacial charge transfer from the GQDs to TiO₂ is the key phenomenon for the enhanced photodegradation of MB. Consecutive degradation cyclic runs to test the highest efficiency and stability of nanocomposites result that the CNF-GQDs-TiO₂ nanocomposites have the fastest photodegradation rate and proved to be the most stable among all. CNT-GQDs-TiO₂, RCNT-GQDs-TiO₂, and CNF-GQDs-TiO₂ nanocomposites show different characteristic radicals \bullet OH, h⁺, and O₂ \bullet^- , respectively, as

revealed by radical quenching experiments. This study is considered to be a platform for nonmetallic QDs and metal oxide semiconductor nanocomposites for green-environment, sustainable energy, and optoelectronic applications.

Author Contributions: J.R.: Conceptualization, Investigation, Methodology, Validation, Data curation, Writing—original draft, Writing—review and editing. U.K.: Conceptualization, Visualization, Formal analysis, Writing—review and editing. M.P.: Writing—review and editing. B.P.: Writing—review and editing. S.-J.P.: Supervision, Funding acquisition, Writing—review and editing. All authors have read and agreed to the published version of the manuscript.

Funding: This research was supported by Korea Electric Power Corporation (Grant number: R21X001-5). This work was also supported by Nano-Convergence Foundation (www.nanotech2020.org (accessed on 1 May 2021)) funded by the Ministry of Science and ICT (MSIT, Korea) & the Ministry of Trade, Industry and Energy (MOTIE, Korea). [Project Name: Development of high-efficiency activated carbon filter for removing indoor harmful elements (VOCs, radon, bacteria, etc.)].

Data Availability Statement: The data is contained within the article.

Conflicts of Interest: The authors declare no conflict of interest.

References

1. Ebrahimi, M.; Samadi, M.; Yousefzadeh, S.; Soltani, M.; Rahimi, A.; Chou, T.C.; Chen, L.C.; Chen, K.H.; Moshfegh, A.Z. Improved solar-driven photocatalytic activity of hybrid graphene quantum dots/ZnO nanowires: A direct Z-scheme mechanism. *ACS Sustain. Chem. Eng.* **2017**, *5*, 367–375. [[CrossRef](#)]
2. Kamran, U.; Park, S.J. Hybrid biochar supported transition metal doped MnO₂ composites: Efficient contenders for lithium adsorption and recovery from aqueous solutions. *Desalination* **2022**, *522*, 115387. [[CrossRef](#)]
3. Kanjwal, M.A.; Barakat, N.A.M.; Sheikh, F.A.; Park, S.J.; Kim, H.Y. Photocatalytic activity of ZnO-TiO₂ hierarchical nanostructure prepared by combined electrospinning and hydrothermal techniques. *Macromol. Res.* **2010**, *18*, 233–240. [[CrossRef](#)]
4. Zhang, Y.; Park, M.; Kim, H.Y.; Park, S.J. In-situ synthesis of graphene oxide/BiOCl heterostructured nanofibers for visible-light photocatalytic investigation. *J. Alloy. Compd.* **2016**, *686*, 106–114. [[CrossRef](#)]
5. Zhang, Y.; Park, M.; Kim, H.Y.; Ding, B.; Park, S.J. In-situ synthesis of nanofibers with various ratios of BiOCl_x/BiOBry/BiOIz for effective trichloroethylene photocatalytic degradation. *Appl. Surf. Sci.* **2016**, *384*, 192–199. [[CrossRef](#)]
6. Kamran, U.; Bhatti, H.N.; Noreen, S.; Tahir, M.A.; Park, S.J. Chemically modified sugarcane bagasse-based biocomposites for efficient removal of acid red 1 dye: Kinetics, isotherms, thermodynamics, and desorption studies. *Chemosphere* **2022**, *291*, 132796. [[CrossRef](#)]
7. Kamran, U.; Bhatti, H.N.; Iqbal, M.; Jamil, S.; Zahid, M. Biogenic synthesis, characterization and investigation of photocatalytic and antimicrobial activity of manganese nanoparticles synthesized from Cinnamomum verum bark extract. *J. Mol. Struct.* **2019**, *1179*, 532–539. [[CrossRef](#)]
8. Gao, L.; Gan, W.; Qiu, Z.; Zhan, X.; Qiang, T.; Li, J. Preparation of heterostructured WO₃/TiO₂ catalysts from wood fibers and its versatile photodegradation abilities. *Sci. Rep.* **2017**, *7*, 1102. [[CrossRef](#)]
9. Nawi, M.A.; Zain, S.M. Enhancing the surface properties of the immobilized Degussa P-25 TiO₂ for the efficient photocatalytic removal of methylene blue from aqueous solution. *Appl. Surf. Sci.* **2012**, *258*, 6148–6157. [[CrossRef](#)]
10. Ji, Z.; Wu, J.; Jia, T.; Peng, C.; Xiao, Y.; Liu, Z.; Liu, Q.; Fan, Y.; Han, J.; Hao, L. In-situ growth of TiO₂ phase junction nanorods with Ti³⁺ and oxygen vacancies to enhance photocatalytic activity. *Mater. Res. Bull.* **2021**, *140*, 111291. [[CrossRef](#)]
11. Hurum, D.C.; Agrios, A.G.; Gray, K.A.; Rajh, T.; Thurnauer, M.C. Explaining the Enhanced Photocatalytic Activity of Degussa P25 Mixed-Phase TiO₂ Using EPR. *J. Phys. Chem. B* **2003**, *107*, 4545–4549. [[CrossRef](#)]
12. Ramakrishnan, V.M.; Natarajan, M.; Santhanam, A.; Asokan, V.; Velauthapillai, D. Size controlled synthesis of TiO₂ nanoparticles by modified solvothermal method towards effective photo catalytic and photovoltaic applications. *Mater. Res. Bull.* **2018**, *97*, 351–360. [[CrossRef](#)]
13. Miao, J.; Zhang, R.; Zhang, L. Photocatalytic degradations of three dyes with different chemical structures using ball-milled TiO₂. *Mater. Res. Bull.* **2018**, *97*, 109–114. [[CrossRef](#)]
14. Ohtani, B.; Prieto-Mahaney, O.O.; Li, D.; Abe, R. What is Degussa (Evonik) P25? Crystalline composition analysis, reconstruction from isolated pure particles and photocatalytic activity test. *J. Photochem. Photobiol. A Chem.* **2010**, *216*, 179–182. [[CrossRef](#)]
15. Luan, Y.; Jing, L.; Meng, Q.; Nan, H.; Luan, P.; Xie, M.; Feng, Y. Synthesis of Efficient Nanosized Rutile TiO₂ and Its Main Factors Determining Its Photodegradation Activity: Roles of Residual Chloride and Adsorbed Oxygen. *J. Phys. Chem. C* **2012**, *116*, 17094–17100. [[CrossRef](#)]
16. Asahi, R.Y.O.J.I.; Morikawa, T.A.K.E.S.H.I.; Ohwaki, T.; Aoki, K.; Taga, Y. Visible-light photocatalysis in nitrogen-doped titanium oxides. *Science* **2001**, *293*, 269–271. [[CrossRef](#)] [[PubMed](#)]

17. Xian, J.; Li, D.; Chen, J.; Li, X.; He, M.; Shao, Y.; Yu, L.; Fang, J. TiO₂ nanotube array-graphene-CdS quantum dots composite film in Z-scheme with enhanced photoactivity and photostability. *ACS Appl. Mater. Interfaces* **2014**, *6*, 13157–13166. [[CrossRef](#)] [[PubMed](#)]
18. Aleksandrak, M.; Adamski, P.; Kukułka, W.; Zielinska, B.; Mijowska, E. Effect of graphene thickness on photocatalytic activity of TiO₂-graphene nanocomposites. *Appl. Surf. Sci.* **2015**, *331*, 193–199. [[CrossRef](#)]
19. Yang, Z.; He, Z.; Wu, W.; Zhou, Y. Preparation of graphene-TiO₂ photocatalysis materials by laser-induced hydrothermal method. *Colloids Interface Sci. Commun.* **2021**, *42*, 100408. [[CrossRef](#)]
20. Ramanathan, S.; Moorthy, S.; Ramasundaram, S.; Rajan, H.K.; Vishwanath, S.; Selvinsimpson, S.; Durairaj, A.; Kim, B.; Vasanthkumar, S. Grape seed extract assisted synthesis of dual-functional anatase TiO₂ decorated reduced graphene oxide composite for supercapacitor electrode material and visible light photocatalytic degradation of bromophenol blue dye. *ACS Omega* **2021**, *6*, 14734–14747. [[CrossRef](#)]
21. Kamran, U.; Park, S.J. Microwave-assisted acid functionalized carbon nanofibers decorated with Mn doped TNTs nanocomposites: Efficient contenders for lithium adsorption and recovery from aqueous media. *J. Ind. Eng. Chem.* **2020**, *92*, 263–277. [[CrossRef](#)]
22. Kamran, U.; Park, S.J. Functionalized titanate nanotubes for efficient lithium adsorption and recovery from aqueous media. *J. Solid State Chem.* **2020**, *283*, 121157. [[CrossRef](#)]
23. Qin, X.; Jing, L.; Tian, G.; Qu, Y.; Feng, Y. Enhanced photocatalytic activity for degrading Rhodamine B solution of commercial Degussa P25 TiO₂ and its mechanisms. *J. Hazard. Mater.* **2009**, *172*, 1168–1174. [[CrossRef](#)] [[PubMed](#)]
24. Wang, D.; Zhao, H.; Wu, N.; El Khakani, M.A.; Ma, D. Tuning the Charge-Transfer Property of PbS-Quantum Dot/TiO₂-Nanobelt Nanohybrids via Quantum Confinement. *J. Phys. Chem. Lett.* **2010**, *1*, 1030–1035. [[CrossRef](#)]
25. Das, G.S.; Shim, J.P.; Bhatnagar, A.; Tripathi, K.M.; Kim, T. Biomass-derived Carbon Quantum Dots for Visible-Light-Induced Photocatalysis and Label-Free Detection of Fe(III) and Ascorbic acid. *Sci. Rep.* **2019**, *9*, 15084. [[CrossRef](#)] [[PubMed](#)]
26. Xie, Y.; Ali, G.; Yoo, S.H.; Cho, S.O. Sonication-Assisted Synthesis of CdS Quantum-Dot-Sensitized TiO₂ Nanotube Arrays with Enhanced Photoelectrochemical and Photocatalytic Activity. *ACS Appl. Mater. Interfaces* **2010**, *2*, 2910–2914. [[CrossRef](#)] [[PubMed](#)]
27. Wang, Q.; Li, J.; Tu, X.; Liu, H.; Shu, M.; Si, R.; Ferguson, C.T.; Zhang, K.A.; Li, R. Single Atomically Anchored Cobalt on Carbon Quantum Dots as Efficient Photocatalysts for Visible Light-Promoted Oxidation Reactions. *Chem. Mater.* **2019**, *32*, 734–743. [[CrossRef](#)]
28. Akbar, K.; Moretti, E.; Vomiero, A. Carbon Dots for Photocatalytic Degradation of Aqueous Pollutants: Recent Advancements. *Adv. Opt. Mater.* **2021**, *9*, 2100532. [[CrossRef](#)]
29. Lee, Y.L.; Chang, C.H. Efficient polysulfide electrolyte for CdS quantum dot-sensitized solar cells. *J. Power Sources* **2008**, *185*, 584–588. [[CrossRef](#)]
30. Pålsson, A.M.B. Toxicity of heavy metals (Zn, Cu, Cd, Pb) to vascular plants. *Wat. Air Soil Poll.* **1989**, *47*, 287–319. [[CrossRef](#)]
31. Bharathi, G.; Nataraj, D.; Premkumar, S.; Sowmiya, M.; Senthilkumar, K.; Thangadurai, T.D.; Khyzhun, O.Y.; Gupta, M.; Phase, D.; Patra, N.; et al. Graphene Quantum Dot Solid Sheets: Strong blue-light-emitting & photocurrent-producing band-gap-opened nanostructures. *Sci. Rep.* **2017**, *7*, 10850. [[PubMed](#)]
32. Mahalingam, S.; Manap, A.; Omar, A.; Low, F.W.; Afandi, N.F.; Chia, C.H.; Abd Rahim, N. Functionalized graphene quantum dots for dye-sensitized solar cell: Key challenges, recent developments and future prospects. *Renew. Sust. Energ. Rev.* **2021**, *144*, 110999. [[CrossRef](#)]
33. Wang, L.; Wang, Y.; Xu, T.; Liao, H.; Yao, C.; Liu, Y.; Li, Z.; Chen, Z.; Pan, D.; Sun, L.; et al. Gram-scale synthesis of single-crystalline graphene quantum dots with superior optical properties. *Nat. Commun.* **2014**, *5*, 5357. [[CrossRef](#)] [[PubMed](#)]
34. Liu, D.; Chen, X.; Hu, Y.; Sun, T.; Song, Z.; Zheng, Y.; Cao, Y.; Cai, Z.; Cao, M.; Peng, L.; et al. Raman enhancement on ultra-clean graphene quantum dots produced by quasi-equilibrium plasma-enhanced chemical vapor deposition. *Nat. Commun.* **2018**, *9*, 193. [[CrossRef](#)] [[PubMed](#)]
35. Maiti, S.; Kundu, S.; Roy, C.N.; Das, T.K.; Saha, A. Synthesis of Excitation Independent Highly Luminescent Graphene Quantum Dots through Perchloric Acid Oxidation. *Langmuir* **2017**, *33*, 14634–14642. [[CrossRef](#)] [[PubMed](#)]
36. Yan, Y.; Chen, J.; Li, N.; Tian, J.; Li, K.; Jiang, J.; Liu, J.; Tian, Q.; Chen, P. Systematic Bandgap Engineering of Graphene Quantum Dots and Applications for Photocatalytic Water Splitting and CO₂ Reduction. *ACS Nano* **2018**, *12*, 3523–3532. [[CrossRef](#)]
37. Li, L.S.; Yan, X. Colloidal Graphene Quantum Dots. *J. Phys. Chem. Lett.* **2010**, *1*, 2572–2576. [[CrossRef](#)]
38. Wang, W.S.; Wang, D.H.; Qu, W.G.; Lu, L.Q.; Xu, A.W. Large Ultrathin Anatase TiO₂ Nanosheets with Exposed {001} Facets on Graphene for Enhanced Visible Light Photocatalytic Activity. *J. Phys. Chem.* **2012**, *116*, 19893–19901. [[CrossRef](#)]
39. Zheng, L.; Su, H.; Zhang, J.; Walekar, L.S.; Molamahmood, H.V.; Zhou, B.; Long, M.; Hu, Y.H. Highly selective photocatalytic production of H₂O₂ on sulfur and nitrogen co-doped graphene quantum dots tuned TiO₂. *Appl. Catal. B* **2018**, *239*, 475–484. [[CrossRef](#)]
40. Shen, K.; Xue, X.; Wang, X.; Hu, X.; Tian, H.; Zheng, W. One-step synthesis of band-tunable N, S co-doped commercial TiO₂/graphene quantum dots composites with enhanced photocatalytic activity. *RSC Adv.* **2017**, *7*, 23319–23327. [[CrossRef](#)]
41. Shaban, M.; Ashraf, A.M.; Abukhadra, M.R. TiO₂ Nanoribbons/Carbon Nanotubes Composite with Enhanced Photocatalytic Activity; Fabrication, Characterization, and Application. *Sci. Rep.* **2018**, *8*, 781. [[CrossRef](#)] [[PubMed](#)]
42. Yi, Z.; Merenda, A.; Kong, L.; Radenovic, A.; Majumder, M.; Dumée, L.F. Single step synthesis of Schottky-like hybrid graphene-titania interfaces for efficient photocatalysis. *Sci. Rep.* **2018**, *8*, 8154. [[CrossRef](#)] [[PubMed](#)]

43. Zhu, L.; Nguyen, D.C.T.; Woo, J.H.; Zhang, Q.; Cho, K.Y.; Oh, W.C. An eco-friendly synthesized mesoporous-silica particle combined with WSe₂-graphene-TiO₂ by self-assembled method for photocatalytic dye decomposition and hydrogen production. *Sci. Rep.* **2018**, *8*, 12759. [[CrossRef](#)] [[PubMed](#)]
44. Umrao, S.; Abraham, S.; Theil, F.; Pandey, S.; Ciobota, V.; Shukla, P.K.; Rupp, C.J.; Chakraborty, S.; Ahuja, R.; Popp, J.; et al. A possible mechanism for the emergence of an additional band gap due to a Ti–O–C bond in the TiO₂–graphene hybrid system for enhanced photodegradation of methylene blue under visible light. *RSC Adv.* **2014**, *4*, 59890–59901. [[CrossRef](#)]
45. Jin, F.L.; Ma, C.J.; Park, S.J. Thermal and mechanical interfacial properties of epoxy composites based on functionalized carbon nanotubes. *Mater. Sci. Eng. A* **2011**, *528*, 8517–8522. [[CrossRef](#)]
46. Yim, Y.J.; Park, S.J. Electromagnetic interference shielding effectiveness of high-density polyethylene composites reinforced with multi-walled carbon nanotubes. *J. Ind. Eng. Chem.* **2015**, *21*, 155–157. [[CrossRef](#)]
47. Donnet, J.B.; Park, S.J. Surface characteristics of pitch-based carbon fibers by inverse gas chromatography method. *Carbon* **1991**, *29*, 955–961. [[CrossRef](#)]
48. Donnet, J.B.; Park, S.J. Anodic surface treatment on carbon fibers: Determination of acid-base interaction parameter between two unidentical solid surfaces in a composite system. *J. Colloid Interface Sci.* **1998**, *206*, 29–32.
49. Das, R.; Rajender, G.; Giri, P.K. Anomalous fluorescence enhancement and fluorescence quenching of graphene quantum dots by single walled carbon nanotubes. *Phys. Chem. Chem. Phys.* **2018**, *20*, 4527–4537. [[CrossRef](#)]
50. Lei, Y.; Hu, J.; Zhang, Z.; Ouyang, Z.; Jiang, Z.; Lin, Y. Photoelectric properties of SnO₂ decorated by graphene quantum dots. *Mater. Sci. Semicond. Process.* **2019**, *102*, 104582. [[CrossRef](#)]
51. Futaba, D.N.; Yamada, T.; Kobashi, K.; Yumura, M.; Hata, K. Macroscopic Wall Number Analysis of Single-Walled, Double-Walled, and Few-Walled Carbon Nanotubes by X-ray Diffraction. *J. Am. Chem. Soc.* **2011**, *133*, 5716–5719. [[CrossRef](#)] [[PubMed](#)]
52. Mo, R.; Lei, Z.; Sun, K.; Rooney, D. Facile Synthesis of Anatase TiO₂ Quantum-Dot/Graphene-Nanosheet Composites with Enhanced Electrochemical Performance for Lithium-Ion Batteries. *J. Adv. Mater.* **2014**, *26*, 2084–2088. [[CrossRef](#)] [[PubMed](#)]
53. Li, D.; Dai, S.; Li, J.; Zhang, C.; Richard-Plouet, M.; Goulet, A.; Granier, A. Microstructure and Photocatalytic Properties of TiO₂–Reduced Graphene Oxide Nanocomposites Prepared by Solvothermal Method. *J. Electron. Mater.* **2018**, *47*, 7372–7379. [[CrossRef](#)]
54. Li, J.; Zhou, S.L.; Hong, G.B.; Chang, C.T. Hydrothermal preparation of P25–graphene composite with enhanced adsorption and photocatalytic degradation of dyes. *J. Chem. Eng.* **2013**, *219*, 486–491. [[CrossRef](#)]
55. Yadav, A.; Yadav, M.; Gupta, S.; Popat, Y.; Gangan, A.; Chakraborty, B.; Ramaniah, L.M.; Fernandes, R.; Miotello, A.; Press, M.R.; et al. Effect of graphene oxide loading on TiO₂: Morphological, optical, interfacial charge dynamics-A combined experimental and theoretical study. *Carbon* **2019**, *143*, 51–62. [[CrossRef](#)]
56. Peng, J.; Gao, W.; Gupta, B.K.; Liu, Z.; Romero-Aburto, R.; Ge, L.; Song, L.; Alemany, L.B.; Zhan, X.; Gao, G.; et al. Graphene Quantum Dots Derived from Carbon Fibers. *Nano Lett.* **2012**, *12*, 844–849. [[CrossRef](#)]
57. Das, R.; Parveen, S.; Bora, A.; Giri, P.K. Origin of high photoluminescence yield and high SERS sensitivity of nitrogen-doped graphene quantum dots. *Carbon* **2020**, *160*, 273–286. [[CrossRef](#)]
58. Qu, D.; Sun, Z.; Zheng, M.; Li, J.; Zhang, Y.; Zhang, G.; Zhao, H.; Liu, X.; Xie, Z. Three Colors Emission from S,N Co-doped Graphene Quantum Dots for Visible Light H₂ Production and Bioimaging. *Adv. Opt. Mater.* **2015**, *3*, 360–367. [[CrossRef](#)]
59. Zhang, Y.; Yang, H.M.; Park, S.J. Synthesis and characterization of nitrogen-doped TiO₂ coatings on reduced graphene oxide for enhancing the visible light photocatalytic activity. *Curr. Appl. Phys.* **2018**, *18*, 163–169. [[CrossRef](#)]
60. Rajender, G.; Kumar, J.; Giri, P.K. Interfacial charge transfer in oxygen deficient TiO₂-graphene quantum dot hybrid and its influence on the enhanced visible light photocatalysis. *Appl. Catal. B* **2018**, *224*, 960–972. [[CrossRef](#)]
61. Ali, M.H.H.; Al-Afify, A.D.; Goher, M.E. Preparation and characterization of graphene–TiO₂ nanocomposite for enhanced photodegradation of Rhodamine-B dye. *Egypt. J. Aquat. Res.* **2018**, *44*, 263–270. [[CrossRef](#)]
62. Thaweechai, T.; Sirisaksoontorn, W.; Poo-Arporn, Y.; Chanlek, N.; Seraphin, S.; Thachepan, S.; Poo-Arporn, R.P.; Suramitr, S. Transparent graphene quantum dot/amorphous TiO₂ nanocomposite sol as homogeneous-like photocatalyst. *J. Nanopart. Res.* **2021**, *23*, 225. [[CrossRef](#)]
63. Sarkar, S.; Raghavan, A.; Giri, A.; Ghosh, S. Graphene Quantum Dots Decorated TiO₂ Nanostructures: Sustainable Approach for Photocatalytic Remediation of an Industrial Pollutant. *ChemistrySelect* **2021**, *6*, 10957–10964. [[CrossRef](#)]
64. Sun, X.; Li, H.J.; Ou, N.; Lyu, B.; Gui, B.; Tian, S.; Qian, D.; Wang, X.; Yang, J. Visible-light driven TiO₂ photocatalyst coated with graphene quantum dots of tunable nitrogen doping. *Molecules* **2019**, *24*, 344. [[CrossRef](#)] [[PubMed](#)]
65. Tian, H.; Shen, K.; Hu, X.; Qiao, L.; Zheng, W. N, S co-doped graphene quantum dots-graphene-TiO₂ nanotubes composite with enhanced photocatalytic activity. *J. Alloy. Compd.* **2017**, *691*, 369–377. [[CrossRef](#)]
66. Bai, X.; Ji, Y.; She, M.; Li, Q.; Wan, K.; Li, Z.; Liu, E.; Li, J. Oxygen vacancy mediated charge transfer expediting over QDs/TiO₂ for enhancing photocatalytic removal of Cr (VI) and RhB synchronously. *J. Alloy. Compd.* **2022**, *891*, 161872. [[CrossRef](#)]
67. Shen, S.; Wang, H.; Fu, J. A nanoporous Three-dimensional graphene aerogel doped with a carbon quantum Dot-TiO₂ composite that exhibits superior activity for the catalytic photodegradation of organic pollutants. *Appl. Surf. Sci.* **2021**, *569*, 151116. [[CrossRef](#)]
68. Leong, K.H.; Fong, S.Y.; Lim, P.F.; Sim, L.C.; Saravanan, P. Physical mixing of N-doped graphene quantum dots functionalized TiO₂ for sustainable degradation of methylene blue. In *IOP Conference Series: Materials Science and Engineering*; IOP Publishing: Bristol, UK, 2018; Volume 409, p. 012009.

69. Safardoust-Hojaghan, H.; Salavati-Niasari, M. Degradation of methylene blue as a pollutant with N-doped graphene quantum dot/titanium dioxide nanocomposite. *J. Clean. Prod.* **2017**, *148*, 31–36. [[CrossRef](#)]
70. Tang, J.; Liu, Y.; Hu, Y.P.; Lv, G.; Yang, C.; Yang, G. Carbothermal Reduction Induced Ti³⁺ Self-Doped TiO₂/GQD Nanohybrids for High-Performance Visible Light Photocatalysis. *Eur. J. Chem.* **2018**, *24*, 4390–4398. [[CrossRef](#)]
71. Kusiak-Nejman, E.; Wanag, A.; Kapica-Kozar, J.; Kowalczyk, Ł.; Zgrzebnicki, M.; Tryba, B.; Przepiórski, J.; Morawski, A.W. Methylene blue decomposition on TiO₂/reduced graphene oxide hybrid photocatalysts obtained by a two-step hydrothermal and calcination synthesis. *Catal. Today* **2020**, *357*, 630–637. [[CrossRef](#)]
72. Deng, Y.; Tang, L.; Feng, C.; Zeng, G.; Wang, J.; Lu, Y.; Liu, Y.; Yu, J.; Chen, S.; Zhou, Y. Construction of Plasmonic Ag and Nitrogen-Doped Graphene Quantum Dots Codecorated Ultrathin Graphitic Carbon Nitride Nanosheet Composites with Enhanced Photocatalytic Activity: Full-Spectrum Response Ability and Mechanism Insight. *ACS Appl. Mater. Interfaces* **2017**, *9*, 42816–42828. [[CrossRef](#)] [[PubMed](#)]
73. Wang, X.Q.; Han, S.F.; Zhang, Q.W.; Zhang, N.; Zhao, D.D. Photocatalytic oxidation degradation mechanism study of methylene blue dye waste water with GR/TiO₂. *MATEC Web Conf.* **2018**, *238*, 03006. [[CrossRef](#)]